Bayesian Dynamic Finite-Fault Inversion: 2. Application to the 2016 Mw6.2 Amatrice, Italy, Earthquake

F. Gallovič[1*], Ľ. Valentová[1], J.-P. Ampuero[2], A.-A. Gabriel[3]

[1] Charles University, Faculty of Mathematics and Physics, Dept. of Geophysics, V Holešovičkách 2, Praha 8, 18000, Czech Republic

[2] Université Cote d'Azur, IRD, CNRS, Observatoire de la Cote d'Azur, Géoazur, 250 rue Albert Einstein, CS 10269 - F 06905 Sophia Antipolis Cedex, France

[3] Ludwig-Maximilians-Universität München, Geophysics, Department of Earth and Environmental Sciences, Theresienstr. 41, 80333 München, Germany

* Contact author: gallovic@karel.troja.mff.cuni.cz

Main point #1:

We apply a new Bayesian dynamic source inversion to the 2016 Amatrice, Italy, earthquake to infer initial stresses and friction properties.

Main point #2:

Ensemble solutions exhibit complex rupture propagation including transient nucleation and pulse like behavior with low radiation efficiency.

Main point #3:

The inferred heterogeneous dynamic models fit very well waveforms recorded at uniquely dense network of near-source seismic stations.

Abstract

In 2016 Central Italy was struck by a sequence of three normal faulting earthquakes with moment magnitude (Mw) larger than 6. The Mw 6.2 Amatrice event (08/24) was the first one, causing building collapse and about 300 casualties. The event was recorded by a uniquely dense network of seismic stations. Here we perform its dynamic source inversion to infer the fault friction parameters and stress conditions that controlled the earthquake rupture. We consider a linear slip-weakening friction law with spatially variable parameters along the fault. The inversion uses a novel Bayesian framework developed in our companion paper, which combines efficient finite-difference dynamic rupture simulations and the Parallel Tempering Monte Carlo algorithm to sample the posterior probability density function. The main advantage of such formulation is that by subsequent analysis of the posterior samples we can infer stable features of the result and their uncertainty. The inversion results in a million of visited models. The preferred model ensemble reveals intriguing dynamic features. The rupture exhibits a slow and irregular nucleation followed by bilateral rupture propagation through two asperities, accelerating towards the heavily damaged city of Amatrice. The stress drop reaches locally 10-15 MPa, with slip-weighted mean of 4-4.5MPa. The friction drop ranges from 0.1 to 0.4. The characteristic slip-weakening distance is the most heterogeneously distributed dynamic parameter, with values of 0.2-0.8m. The radiation efficiency was rather low, 0.2, suggesting that approximately 80% of the total available energy was spent in the fracture process, while just 20% was radiated by seismic waves.

1. Introduction

In 2016 Central Italy was struck by three Mw>6 earthquakes associated with normal faulting with NW-SE strike and dip towards SW, which is the prevalent style of faulting in the area (Chiaraluce et al., 2017). The first strong earthquake of the sequence (08/24, Mw 6.2) caused building collapse and about 300 casualties. Two months later, the next event (10/26, Mw 6.1) extended the seismogenic volume to the NW, and 4 days later (10/30, Mw 6.5) the largest event hit the same area. The events were recorded by a uniquely dense network of near-source seismic stations. Kinematic source inversion of all the three events by Pizzi et al. (2017) using the method by Gallovič et al. (2015) suggests complementarity of their ruptures with possible relations to the growth of the normal fault system in the area. Aochi and Twardzik (2019) performed an iterative search for dynamic rupture parameters of two seismogenic asperities by comparison with near-field ground motions.Other (kinematic) finite-fault source inversion models (e.g., Cirella et. al., 2018; Tinti et al., 2016; Cheloni et al., 2017) based on geological, geodetic and seismic data reveal a rather large degree of non-uniqueness, which is typical of ill-constrained source inversion problems.

Kinematic source inversions, which infer the coseismic slip history along the fault, provide only limited information on the physical processes driving the rupture. Instead, dynamic source inversion is a systematic approach by which the distributions of stress and parameters of an assumed friction law along the fault are optimized so that the resulting dynamic rupture model produces ground motions that fit the observed data. Earthquake dynamic modeling is a key element for understanding the physics of earthquake occurrence, nucleation, propagation and arrest. In the last decades there has been substantial progress in dynamic rupture modeling, so that recent studies of selected earthquakes have shed new light on earthquake processes (e.g. Ulrich et al., 2018). Nevertheless, just few attempts of full dynamic source inversion have been made so far (Corish et al., 2007; Peyrat and Olsen, 2004; Fukuyama and Mikumo, 1993) due to its high computational burden.

In our companion paper (Gallovič et al., submitted to JGR) we introduce a novel Bayesian dynamic source inversion method. Here we apply it to infer physical parameters and stress conditions that governed the 2016 Mw 6.2 Amatrice earthquake. We adopt the fault geometry assumed by Pizzi et al. (2017). We consider a heterogeneous prestress and a linear slip-weakening friction law parameterized by along-fault distributions of the difference between static and dynamic friction coefficients (friction drop) and slip-weakening distance D_c. The spatial distributions of those parameters are determined by a Monte Carlo Markov Chain approach in a nonlinear dynamic inversion that aims at fitting displacement waveforms at 20 stations within 50 km fault distance (Fig. 1) at frequencies lower than 1 Hz. After discussing the inversion results, we simulate the wavefield at frequencies up to 5 Hz, demonstrating that the main features of the observed velocity waveforms are captured by the synthetics, especially at stations where site effects are presumably insignificant.

2. Method

Here we give an overview of the main features of the Bayesian dynamic source inversion introduced in our companion paper. Therein the approach is validated on a community benchmark test based on a spontaneous dynamic rupture model (Mai et al., 2016).

We assume a planar fault governed by the linear slip-weakening friction law (Fig. 2A) embedded in an elastic medium. The 3D elastodynamic equation and dynamic rupture are solved in a relatively small box covering the fault using a finite difference method (code FD3D by Madariaga et al., 1998, with thin fault boundary conditions; Ruiz and Madariaga, 2011; Twardzik et al., 2014). The computational box can be made small because we do not need to include the station; the station waveforms are calculated externally as specified further. Pure dip slip on a vertical fault is considered, for computational efficiency. A one-dimensional layered elastic velocity structure is assumed (Fig. 3). The variable model parameters (initial stress, friction drop and D_c) are parameterized by values on control points covering the fault (Fig. 2C), from which they are bilinearly interpolated onto the denser FD computational grid (for the actual grid size values see Tab. 1). The dynamic simulation results in slip rate histories along the fault. Following the seismological representation theorem (Aki and Richards, 2002), the slip rate functions are then convolved with Green's functions representing impulse responses of the medium. The Green's function are pre-calculated at stations inside and outside the finite-difference domain using a different method and software, Axitra (Bouchon, 1981; Coutant, 1989; Kennett & Kerry, 1979). It is based on the discrete wave number and matrix methods, adopting the correct (dipping) fault geometry. As a result, synthetic seismograms at specified stations are obtained. The misfit relative to observations is evaluated as the weighted L2 norm of the difference between observed and simulated displacement waveforms after applying the same, optimal time shift uniformly to all stations and components.

While the use of a vertical fault in the dynamic rupture simulation seems a very crude approximation of the actual 45° dipping fault geometry, this approximation affects only the dynamic rupture simulation and not the calculation of synthetic seismograms. We have tested the validity of our approximation by comparing rupture propagation simulations by FD3D and WaveQLab3D (Duru and Dunham, 2016) that uses summation-by-parts (SBP) 6th-order finite difference operators on boundary-conforming curvilinear mesh, thus accounting for the fault dip. Both methods include free surface boundary condition. As shown in Appendix A for our best-fitting model, the rupture models and generated seismograms agree sufficiently well. For more discussion on this point see Appendix A.

Model optimization is performed using a Monte Carlo Markov Chain (MCMC) method called Parallel Tempering (e.g., Falcioni and Deem, 1999; Sambridge, 2013). The method is similar to the classical simulated annealing, as the posterior PDF is modified by a temperature T. Instead of a gradual decrease in T, the Parallel Tempering method employs a set of Markov chains simultaneously advancing at various temperatures. To ensure sufficient sampling of the model space, the chains are allowed to exchange temperature values following the adapted Metropolis-Hastings acceptance rule (Sambridge, 2013). This way, we obtain samples of the posterior PDF function, whose parameters can be further analyzed in a statistical sense.

3. Data, velocity model and fault geometry

We use strong motion data recorded by the Rete Accelerometrica Nazionale and the Rete Sismometrica Nazionale, operated by the Italian Department of Civil Protection and the Istituto Nazionale di Geofisica e Vulcanologia, respectively. The records were downloaded from the Engineering Strong-Motion database (Luzi et al., 2016a; Luzi et al., 2016b). For the inversion we use all 20 three-component strong motion waveforms recorded within 50 km from the fault.

We filtered the data by a fourth-order causal Butterworth filter between 0.05 and 1 Hz for the closest stations AMT and NRC, and between 0.05 and 0.5 Hz for the other stations (with the exception of station RQT where the 0.1-0.5 Hz band was considered). The high-pass filtering removes low-frequency (mostly instrumental) noise from the data, while the low-pass filter is dictated by limitations of our synthetic Green’s functions due to imperfect velocity model (Hallo and Gallovič, 2016) and imprecise location and geometry of the fault (Ragon et al., 2018 and 2019). The waveforms are not weighted; implicitly, the station weights are given by the recorded amplitudes, which are higher at the closest stations. We consider the data error standard deviation is equal to 0.1 m, which is twice larger than considered by Pizzi et al. (2017), to account for the uncertainty of the velocity model, fault geometry and also for inaccuracies of the dynamic simulation method.

The causative fault plane of the Amatrice earthquake was thoroughly investigated by Tung and Masterlark (2018). Using static 3D Finite-Element Modeling they found that a listric fault geometry provides the best fit of the observed InSAR data. Nevertheless, due to limitations of the forward solver we use a planar fault inferred from seismological data by Pizzi et al. (2017) by kinematic finite-fault inversion with grid search over the fault plane location, fault geometry (strike and dip), and slip direction (rake). To reduce the computational cost, we slightly adjusted the size of the optimal fault by Pizzi et al. (2017) from 36x12 km to 30x14 km.

Synthetic Green’s functions are calculated for the 1-D velocity model (Fig. 3) adopted from Gallovič and Zahradník (2012) and Ameri et al. (2012), who used it for low-frequency and broadband modeling of the 2009 L’Aquila earthquake, respectively. This velocity model was also used by Pizzi et al. (2019) for the kinematic inversion of the 2018 Amatrice earthquake. The Green’s functions (and thus the synthetics) are filtered in the same way as the data for consistency.

4. Dynamic inversion setup and strategy

The grid parameters and normal stress profile considered in the present study are listed in Tab. 1, along with a priori bounds on the values of the dynamic parameters. In addition, since we have prior approximate information about the hypocenter position, each newly proposed model in the MCMC sampling is allowed to have negative strength excess (the difference between static frictional strength and initial shear stress) only in a prescribed nucleation area (see Tab. 1). Any model that violates this condition is discarded and a new proposal model is generated without running an expensive dynamic simulation. In the dynamic simulations the negative strength excess area initiates the rupture propagation. Depending on dynamic parameters within and around this initial patch the rupture may or may not continue to propagate outside the nucleation area in a spontaneous matter.

Regarding the initial model for the dynamic inversion, we explain in the companion paper that the MCMC sampling cannot start from very random models because the sampling would require an unbearable amount of trial dynamic rupture simulations to find the proper part of the model space with meaningful rupture models. Indeed, in most of the model space the rupture would not even start or would start, but in an unsuitable manner (e.g, unilateral, too fast or slow or with incorrect seismic moment) resulting in poor fit to the data. To avoid this, we follow the strategy outlined in the companion paper, combining prior information on the nucleation area and using a starting model based on a preliminary kinematic slip inversion as detailed below.

We build the initial model from the slip model determined by linear kinematic source inversion using the code LinSlipInv (Gallovič et al., 2015) as in Pizzi et al. (2017). The stress drop distribution is computed from the final slip distribution using the elastostatic formulas for dislocations in a homogenous half space by Okada (1992). The initial stress is set equal to the dynamic frictional strength plus the resulting stress drop. The other dynamic parameters are set manually to obtain a rupture model with positive variance reduction (VR). Achieving that required to prevent the rupture from reaching the surface (which would largely overestimate ground motions) by setting larger values of the static friction and D_c in the upper ~5 km. We also limited the rupture depth by prescribing larger values of the dynamic parameters at the bottom of the fault. We used the parallel tempering inversion to improve this dynamic model in terms of waveform fit. In the inversion even the previously prescribed values at shallow depths and fault edges are allowed to change. During this procedure we stopped the inversion several times, selected the best-fitting model and used it as a new starting model. In some cases we also manually changed dynamic parameters to improve the fit especially at the closest stations, thus guiding the Monte Carlo sampler to reach faster the part of the model space with well-fitting rupture models. For example, we increased the prestress of the SE asperity and decreased D_c to increase the slip and rupture speed, which in turn amplifies waveform amplitudes at the AMT station; the inversion was then rerun. Once VR exceeded ~0.5, we started the final extensive exploitation of the model space that resulted in the ensemble of posterior samples investigated in the next section.

In the exploitation phase we used in total ~10,000 MCMC chains (with about 1/5 at temperature T=1) that visited ~1,000,000 models. Every 10th step of the Markov chain the models at T=1 were saved. The final set consists of ~5000 model samples representing the random draws from the posterior PDF. In all the calculations we combined runs on the Xeon supercomputer cluster IT4I and our local farm of 10 GPU cards.

5. Results

In the following we discuss first the properties of the best-fitting model (maximum likelihood estimate) to give an idea about the rupture properties, waveform fit and the controlling dynamic parameters. Then, since the inversion result is to be understood in the Bayesian framework as a family of solutions, we discuss uncertainties of both kinematic and dynamic parameters of the sampled posterior PDF.

5.1. Best-model properties

Fig. 4A displays the slip distribution and slip rate functions of the best-fitting dynamic rupture model with variance reduction VR=0.62. The slip rate snapshots showing the rupture evolution in time are presented in Fig. 4B. Fig. 5 shows along-fault distributions of the stress drop, rupture time, rupture speed and rise time (calculated as a ratio of final slip and peak slip rate). In agreement with published kinematic rupture models, our best-fitting dynamic model exhibits a bilateral rupture propagation with very weak nucleation. Indeed, during the first 2-3 seconds the rupture almost ceases, and is followed by a fast recovery of the spontaneous rupture process. The rupture propagates first towards SE at relatively high speed and with short rise times (Fig. 5). During this period, the rupture propagates at smaller speed, smaller peak slip-rates and with longer rise times also towards NW. Before stopping in the SE direction, the NW part of the rupture accelerates, increasing the peak slip rates and shortening the rise times. The largest slip is located in the NW part of the fault. The major slip area is depleted of on-fault aftershocks, consistent with stress release.

In Fig. 4C we compare synthetic and observed displacement waveforms. The highest amplitudes observed at station AMT, well fitted by our model, are related to the energetic rupture propagation towards the site, suggesting a strong directivity effect. Contrarily, at the other nearest station, NRC, the waveform fit is not so good, perhaps due to the simplification of the fault geometry which affects more strongly the nearest stations. For the remaining, more distant stations the waveform fit is excellent.

Fig. 6 shows the dynamic parameters of this particular source model. Note that dynamic parameters outside the ruptured area (delimited by the black contour in Fig. 6) are not constrained by the inversion (see Sec. 5.2). The first two rows of Fig. 6 contain the distributions of relative prestress τ_i, friction drop and D_c. The prestress presented is relative to the dynamic frictional strength of the fault; in the rupture area, it is an estimate of the coseismic stress drop. In particular, the prestress is elongated horizontally, having a maximum of 12 MPa SE of the hypocentral area and two additional minor local maxima of ~7 MPa located further in the NW and SE directions from the nucleation. Within the rupture area the friction drop values range from 0.1 to 0.4. The largest values are located in a profound heterogeneity located close to the hypocenter in the SE direction. The characteristic slip-weakening distance D_c is the most heterogeneously distributed dynamic parameter, with values between 0.2 and 0.8 m. The lowest values of D_c are located in a narrow, horizontally elongated patch, approximately at the middle depth of the rupture. This patch lacks on-fault aftershocks, presumably due to the fact that the stress was released by the mainshock slip.

Next we discuss several derived quantities calculated from the distribution of the inverted dynamic parameters. In particular, the distribution of strength excess (τ_s-(τ_i+τ_d), see Fig. 2) displayed in Fig. 6 shows that the nucleation region is only weakly overstressed (~ -0.1 MPa). Outside the nucleation area the strength excess is approximately constant, (~ 4 MPa). The region of large prestress located SE of the hypocenter is thus compensated by a larger strength. The strength excess increases strongly at the edges of the ruptured area to values larger than 10 MPa, which causes the rupture to stop.

The along-strike prolongation of the rupture can be observed also in the distribution of the so-called *S* parameter, characterizing the on-fault stress state (Andrews, 1976), defined as

$$S = \frac{\tau_s-(\tau_i+\tau_d)}{(\tau_i+\tau_d)-\tau_d} = \frac{(\tau_s-\tau_d)-\tau_i}{\tau_i} = \frac{(\mu_s-\mu_d)\sigma_n-\tau_i}{\tau_i}. \qquad (1)$$

For the definition of the stresses and friction coefficients in Eq. (1) see Fig. 2A. The *S* parameter ranges between 0.1 and 0.4 in a patch much narrower than the rupture extent. We note that for

S values as small as 0.1-0.4 the rupture would go supershear on a homogeneous and unbounded fault (Andrews, 1976, Dunham, 2007). However, in our model this behavior is prevented by early stopping (arrest) phases due to the limited width of the rupture (Dunham, 2007; Beroza and Mikumo, 1996). Outside of this patch the S parameter quickly increases to values larger than 1. Nevertheless, the rupture propagates even to those areas, but with smaller slip values.

For the best-fitting model Fig. 6 also shows the along-fault distributions of breakdown work density, also known as fracture energy, defined in Fig. 2 as

$$G_b = \frac{1}{2}(\tau_s - \tau_d)D_c, \qquad (2)$$

(Ripperger et al., 2007; Kanamori and Brodsky, 2004). The mean breakdown work density is 1.1 MJ/m^2. This value is comparable to that inferred for past earthquakes of similar magnitude or similar average slip of 0.67 m (Viesca and Garagash, 2015), but the uncertainty of those estimates is large. The total breakdown work (integrated along the fault) is 1.6×10^{14} J.

As discussed in the methodological sections, we use several approximations in the dynamic rupture simulation when performing the inversion. To confirm that the best-fitting model is simulated correctly, we have recalculated it using the more advanced code WaveQLab3D (Duru and Dunham, 2016), a 6th-order accurate finite difference code, which has been verified in many community dynamic rupture benchmarks (Harris et al., 2018). In the WaveQLab3D simulation we respect the actual dipping fault geometry. We present the comparison between the FD3D and WaveQLab3D solutions in terms of slip rates and radiated waveforms in Appendix A1. Compared to our approximate solution, the WaveQLab3D modeling results in only slightly faster rupture propagation, providing slightly larger displacement amplitudes (Fig. A1). Nevertheless, in the Bayesian approach the best-fitting model cannot be considered as the closest one to the true model. This is due to the random errors caused by both observational errors and modeling errors due to the use of the fast dynamic solver, as demonstrated on a synthetic test in the companion paper. Instead, the result of the inversion is not one preferred model but an ensemble, the whole set of posterior PDF samples. Therefore, in the following section we analyze statistical properties of the inferred ensemble.

5.2. Ensemble properties

Fig. 7 shows histograms of various parameters derived from the ensemble of rupture models, considering only models with posterior probability density value larger than 2% of the posterior PDF maximum (~5000 models). The scalar seismic moment covers the value $2.5\text{x}10^{18}$ Nm provided by the Harvard CMT project. The slip-weighted mean stress drop ranges from 4.0 to 4.5 MPa, which falls within the range of stress drops in Central Italy as reported by Bindi et al. (2018) and Pacor et al. (2016). The nucleation zone area spans the range of 2-10 km^2 with mean nucleation overstress up to 1.5 MPa. The total fracture energy E_d and radiated energy E_r calculated according to Ripperger et al. (2007) are of $1.5\text{x}10^{14}$ Nm and $5\text{x}10^{13}$ Nm, respectively. Aochi and Twardzik (2019) inferred ~2 times smaller fracture energy. Nevertheless, they also obtained ~2 times smaller ruptured area, implying that the fracture energy rates are consistent with our rupture ensemble.

The ratio between radiated energy and seismic moment (scaled energy, e.g. Kanamori and Brodsky, 2004) is approximately $1.7\text{x}10^{-5}$ ($1.2\text{-}2.2\text{x}10^{-5}$). The radiation efficiency, defined as

$$\eta_r = \frac{E_r}{E_r + E_b}, \qquad (5)$$

spans the range of 0.15-0.25, suggesting that approximately 80% of the total available energy was spent in the fracture process, while just 20% was radiated by seismic waves.

Fig. 8A shows distributions of mean slip, stress drop and rise time values along the fault and their uncertainty expressed as twice the standard deviation σ. In all cases the uncertainty is largest at the edge of the rupture (see the black contour of the mean slip in Fig. 8A), because the rupture extent varies among the inferred source models. Indeed, the rupture extent variability can be appreciated from Fig 8B, which shows contours of slip of the individual accepted models. Note that some of the models reach the free surface, but with rather small slip values. The mean slip has maximum amplitude of approximately 1.2 m and its uncertainty reaches 0.1 m, i.e. approximately 10% of the mean. The mean stress drop is ~12 MPa. Its relative variability is around 10% in the middle and NW parts of the fault. It reaches approximately 20-30% in the SE part of the fault, perhaps because this part of the inferred rupture is strongly controlled by a single nearby AMT station. The rise time distribution suggests that the rupture starts as a crack, with larger rise times (~4 s) in the middle of the fault, and then becomes a pulse, with short rise times (~0.2 s). This result is supported by the uncertainty analysis: the relative variability is around 20% both for the large and short rise times. Notably, rupture speed exhibits overall a comparably large variability of 25%.

Fig. 9 shows mean values of dynamic parameters and their scatter in terms of twice the standard deviation σ. The mean values are very close to the values of the best-fitting model (compare with Fig. 6). The uncertainties (Fig. 9) are irregularly distributed. They have larger values in areas with large mean values, suggesting approximately constant relative uncertainty. The relative standard deviation of prestress and friction drop (and thus strength excess) is approximately 20%, while that of D_c reaches ~50%.

6. Discussion

Our inferred set of models of the 2016 Amatrice earthquake (including the best-fitting model) agrees with published kinematic and dynamic models in a general sense. They exhibit bilateral rupture propagation and have two slip maxima away from the rupture nucleation (Pizzi et al., 2017; Cirella et al., 2018; Aochi and Twardzik, 2019). The latter feature has been also revealed in geodetic inversion by Huang et al. (2018). Rupture propagation along the SE portion of the fault contributed to the ground motion amplification in Amatrice, which experienced significant damage and casualties, and recorded peak acceleration reaching 0.8 g (Fiorentino et al., 2018). As identified by Ren et al. (2017), at larger distances the directivity effect was dominated by the NW rupture propagation along the spatially larger asperity with larger slip.

Our dynamic models exhibit relatively smooth slip distribution in accord with the models by Pizzi et al. (2017) and Huang et al. (2018). They differ from the model of Tinti et al. (2016), in which the slip is composed of distinct smaller patches. Such differences among kinematic models can be attributed to the strength of smoothing constraints applied in the kinematic inversion methods. The relative smoothness of the slip distribution we obtain is, however, the result of the dynamic modeling. Indeed, in dynamic modeling of the Amatrice earthquake by Aochi and Twardzik (2019), the authors had to add smaller rupture pathways between the NW and SE asperities in order to connect them with the nucleation patch. Therefore, a model with distinct separated slip patches would be hardly justifiable with the present friction law and model parameterization.

In terms of dynamic parameters, the slip-weighted mean stress drop falls in between 4 and 4.5 MPa, reaching locally 10 to 15 MPa. These values are consistent with stress drops inferred by Aochi and Twardzik (2019). The friction drop ranges from 0.1 to 0.4 and the characteristic slip-weakening distance varies significantly between 0.2 and 0.8 m along the fault. The radiation efficiency is estimated ~0.2, i.e. rather low, suggesting that approximately 80% of the total available energy was spent in the fracture process, while just 20% was radiated by seismic waves. Such relatively small radiation efficiency suggests relatively weak high-frequency radiation for the given magnitude. Indeed, Lanzano et al. (2016) computed between-event terms with respect to Italian ground motion prediction equations for the Amatrice earthquake (see Fig. 8 therein). They demonstrate that the high-frequency between-event error is smaller than the corresponding term at low-frequency, suggesting that the amount of high-frequency energy was smaller than empirically expected for the given magnitude. This is thus in agreement with our finding that the energy budget of the Amatrice earthquake rupture was dominated by the fracture process.

6.1. Weak nucleation of the earthquake

The inferred model of the 2016 Amatrice earthquake is characterized by a relatively weak nucleation, where the rupture almost dies out before restarting and extending to the full Mw6.2 earthquake. Therefore, the rupture propagation is purely spontaneous in the sense that the nucleation patch did not give much ‘push’ to the rupture onset.

Weak nucleation suggests that the eventual earthquake size is not determined at the nucleation stage. Instead, the progress of the rupture process is controlled by subtle spatial heterogeneities of the local readiness of the fault to rupture. Such character of the rupture process has important implications for the (im)possibility of prediction of the earthquake magnitude from the beginning of the observed seismograms. This in turn has implications for early warning systems (Murphy and Nielsen, 2009). Nevertheless, to test if more solid evidence for such behavior exists, systematic dynamic inversions of many other events would be needed.

6.2. Structural control on the earthquake rupture

In our approach we do not distinguish between the classical asperity and barrier dynamic rupture models Di Carli et al. (2010). Due to the parameterization of the dynamic source properties the rupture can be locally stopped by low prestress, high strength, but also large Dc (where the latter two combine in large Gc). This is evident when inspecting lFig. 9 for the possible role of the various dynamic parameters in constraining the rupture extent. In particular, large values of strength excess surround the rupture from the top and bottom, due to both low prestress and large friction drop. However, in the along strike direction, the strength excess outside the rupture zone is lower. Moreover, in the NW part it has large uncertainty. Another parameter controlling rupture arrest is the characteristic slip weakening distance D_c. It is small in the SE part, suggesting that rupture stopped there dynamically due to the rather low stress drop (i.e. low prestress) providing insufficient energy for the rupture to extend.

In the NW the situation is different. While strength excess and prestress are basically constant at the NW inner edge of the rupture, D_c is larger even when taking its uncertainty into account (Fig. 9). Pizzi et al. (2017) suggest that the apparent listric shape of the on-fault aftershocks are associated with the intersection of the normal fault with the Sibillini Mountains Thrust (MST) ramp. In 3D the aftershocks delineate a spoon-like structure corresponding to the MST. The MST likely behaves as a structural barrier at depth, controlling the termination of the Amatrice earthquake rupture. This suggests that the structural complexity due to the intersection with the MST stopped the rupture in the NW, although not abruptly. This structural effect is reproduced in our dynamic model by making D_c larger.

6.3. Style of rupture propagation

The rise time distribution (Fig. 8A) suggests that the rupture starts as a crack, with larger rise times (~4 s) in the middle of the fault. Then it continues as a pulse, with short rise times (~0.2 s). This result is supported by the uncertainty analysis.

Remarkably, rupture propagation in the form of slip-pulses is not naturally expected from dynamic rupture simulations that assume linear-slip weakening friction on planar faults and smoothly distributed initial stresses and frictional properties. As shown in theoretical studies by Beroza and Mikumo (1996) and Oglesby and Day (2002), pulse-like rupture in linear-slip weakening models can arise from fault heterogeneities. Therefore, both the transient nucleation and the pulse-like rupture propagation are here enabled by a sensitive balance of the inhomogeneities in the inferred stress and friction parameters making the rupture zone narrower, and thus producing early stopping phases. We note that for other, more complex friction laws (such as strong-velocity weakening; e.g. Gabriel et al., 2012 and 2013) and/or in the presence of structural complexity (such as damage zone effects; e.g. Huang et al., 2011 and 2014, or geometric complexity; e.g., Wollherr et al., 2019), pulse-like rupture propagation is more typical. In this sense, the strongly inhomogeneous friction properties in our models, especially D_c, represents rather a proxy for unaccounted dynamic features. Therefore, dynamic models with geometrically complex fault geometries, including listric and fractally rough surfaces, and other friction laws (which can generate pulses without stress heterogeneity) shall be explored in the future.

6.4. Prediction of broadband ground motions

An alluring property of the dynamic modeling is that given the dynamic parameters, one can calculate the waveforms up to much higher frequencies than considered in the inversion (<1 Hz). We can then examine to what extent our dynamic model can explain broadband recordings. We calculate the waveforms from the best-fitting model in the frequency range 0.05-5.0 Hz using the WaveQLab3D code and the pre-calculated Green's functions in the 1D velocity model. The comparison of velocity waveforms is displayed in Fig. 10.

The fit is surprisingly good, considering the large number of stations, their almost perfect azimuthal coverage and the richness of the waveform shapes. The fit is exceptionally good at stations with presumably weak high-frequency site effect. This is demonstrated also in Fig. 11 showing comparison of the broadband seismograms in the Fourier domain for four selected stations. The first two selected stations (PZI1 and ANT) rank among the best fitted, while the other two (SNO and FOS) serve as examples of stations with clear site effects exhibited by spectral amplification above ~1 Hz. The latter feature is obviously not captured by our simplified 1D velocity model. Interestingly, the fit is also relatively poor for the nearest stations. This can be attributed to the oversimplified rupture geometry, to which the nearest stations are most sensitive.

This exercise demonstrates the viability of fully dynamic rupture models governed by linear slip-weakening friction combined with synthetic Green's functions to explain the major characteristics of the observations at near-source distances. This supports the possibility of using dynamic models for strong motion prediction, e.g., for physics-based ground motion simulations, provided correct dynamic properties are prescribed and computational cost is affordable.

7. Conclusions

We have applied a newly developed dynamic source inversion to the well recorded 2016 Mw6.2 Amatrice, Central Italy, earthquake, assuming a linear slip weakening friction law on a planar fault. Generally speaking, finding the optimal distribution of dynamic parameters is computationally challenging due to the strongly non-linear relation between model parameters and seismograms. We formulate the inverse problem in a Bayesian framework, utilizing parallel tempering Monte Carlo Markov Chain approach (Sambridge, 2013) to sample the posterior probability density function. Our approach to the dynamic inversion is tractable thanks to the combination of relatively fast (yet not perfectly precise) dynamic rupture solver and the use of prior constraints on the nucleation area (to avoid running dynamic simulations for models that would provide a poor fit to the data).

In accordance with other published kinematic and dynamic models, our rupture models exhibit bilateral rupture propagation with two asperities, and pronounced propagation towards the city of Amatrice. The latter feature is most likely responsible for the damaging strong motions with peak acceleration reaching 0.8 g (Fiorentino et al., 2018). The slip-weighted mean stress drop is between 4 and 4.5 MPa. The friction drop ranges from 0.1 to 0.4 and the characteristic slip-weakening distance varies significantly between 0.2 and 0.8 m along the fault. The radiation efficiency is estimated ~0.2, suggesting that the energy budget of the Amatrice earthquake rupture was dominated by the fracture process. This explains the observed relatively weak high-frequency radiation identified from comparison with Italian ground motion prediction equations (Lanzano et al., 2016).

Since the dynamic inversion also provides kinematic parameters of the rupture, it can be also viewed as a kinematic inversion constrained by the assumed friction law. This is advisable as kinematic inversions are highly non-unique (Mai et al., 2016; Gallovič and Ampuero, 2015; Gallovič and Zahradník, 2011).

The present dynamic inversion opens an avenue for systematic analysis of a large number of earthquakes. Subsequent statistical analysis of the resulting dynamic parameters could allow to study relations between fault strength and slip to validate fault weakening models, and to dynamically constrain rupture simulations for practical applications such as seismic hazard assessment.

Acknowledgement

We thank L. Hanyk and J. Premus for their help with the software development, and K. Duru for providing us with the WaveQLab3D solver and for his guidance in its usage. We are grateful to Olaf Zielke and an anonymous reviewer for their valuable comments that improved the presentation of our results. Most of the calculations were carried out on Salmon supercomputer (Ostrava), supported by the Ministry of Education, Youth and Sports from the Large Infrastructures for Research, Experimental Development and Innovations project “IT4Innovations National Supercomputing Center – LM2015070” (IT4I supercomputer). F. G., L. V. and A.-A. G. acknowledge financial support through the bilateral project of the Czech Science Foundation and DFG, no. 18-06716J and GA 2465/2-1, respectively. J.-P. A. acknowledges support by the French government, through the UCAJEDI Investments in the Future project managed by the National Research Agency (ANR) with the reference number ANR-15-IDEX-01. A.-A. G. acknowledges support by the European Union’s Horizon 2020 research and innovation program (ExaHyPE, grant no. 671698 and ChEESE, grant no. 823844), by the Volkswagen Foundation (ASCETE, grant no. 88479) and by KAUST-CRG (GAST, grant no. ORS-2016-CRG5-3027 and FRAGEN, grant no. ORS-2017-CRG6 3389.02).

References

Aki, K., and P. G. Richards (2002). Quantitative Seismology, University Science Books, Sausalito, California.

Ameri, G., F. Gallovic, and F. Pacor (2012). Complexity of the Mw 6.3 2009 L'Aquila (Central Italy) earthquake: 2. Broadband strong-motion modeling, J. Geophys. Res., 117, B04308.

Andrews, D. J. (1976). Rupture velocity of plane strain shear cracks, J. Geophys. Res., 81(32), 5679-5687.

Aochi, H., and C. Twardzik (2019). Imaging of Seismogenic Asperities of the 2016 ML 6.0 Amatrice, Central Italy, Earthquake Through Dynamic Rupture Simulations, Pure Appl. Geophys, in press.

Beroza, G. C., and Mikumo, T. (1996). Short slip duration in dynamic rupture in the presence of heterogeneous fault properties, J. Geophys. Res. 101, 22449-22460.

Bindi, D., D. Spallarossa, M. Picozzi, D. Scafidi, and F. Cotton (2018). Impact of Magnitude Selection on Aleatory Variability Associated with Ground-Motion Prediction Equations: Part I—Local, Energy, and Moment Magnitude Calibration and Stress-Drop Variability in Central Italy. Bull. Seism. Soc. Am. 108, 1427-1442.

Bouchon, M. (1981). A simple method to calculate Green's functions for elastic layered media, Bull. Seism. Soc. Am., 71, 959–971.

Chiaraluce, L., R. Di Stefano, E. Tinti, L. Scognamiglio, M. Michele, E. Casarotti, M. Cattaneo, P. De 650 Gori, C. Chiarabba, G. Monachesi, A. Lombardi, L. Valoroso, D. Latorre, and S. Marzorati (2017). The 2016 Central Italy Seismic Sequence: A First Look at the Mainshocks, Aftershocks, 652 and Source Models, Seismol. Res. Lett., 88, 757-771.

Cirella, A., G. Pezzo, and A. Piatanesi (2018). Rupture kinematics and structural-rheological control of the2016 Mw6.1 Amatrice (central Italy) earthquake from joint inversion of seismic and geodetic data, Geophys. Res. Lett. 45, 12,302–12,311.

Corish, S. M., Bradley, Ch. R., Olsen, K. B. (2007). Assessment of a Nonlinear Dynamic Rupture Inversion Technique Applied to a Synthetic Earthquake, Bull. Seism. Soc. Am. 97, 901-914.

Coutant, O. (1989). Program of numerical simulation AXITRA, Tech. rep., Lab. de Geophys. Interne et Tectonophys., Grenoble, France.

Di Carli, S., C. François-Holden, S. Peyrat, and R. Madariaga (2010). Dynamic inversion of the 2000 Tottori earthquake based on elliptical subfault approximations, J. Geophys. Res. 125, B12328.

Dunham, E. M. (2007). Conditions governing the occurrence of supershear ruptures under slip-weakening friction, J. Geophys. Res. 112, B07302.

Duru, K., and E. M. Dunham (2016). Dynamic earthquake rupture simulations on nonplanar faults embedded in 3D geometrically complex, heterogeneous Earth models, J. Comp. Phys. 305, 185–207.

Falcioni, M., and M. W. Deem (1999). A biased Monte Carlo scheme for zeolite structure solution, J. Chem. Phys. 110, 1754-1766.

Fiorentino, G., A.Forte, E. Pagano, F. Sabetta, C. Baggio, D. Lavorato, C. Nuti, and S. Santini (2018). Damage patterns in the town of Amatrice after August 24th 2016 Central Italy earthquakes, Bull. Earthquake Eng., 16, 3, 1399-1423.

Fukuyama, E. and T. Mikumo (1993). Dynamic rupture analysis: Inversion for the source process of the 1990 Izu-Oshima, Japan, earthquake, J. Geophys. Res., 98, 6529-6542.

Gabriel, A. A., J. P. Ampuero, L. A. Dalguer, and P. M. Mai (2012). The transition of dynamic rupture styles in elastic media under velocity-weakening friction J. Geophys. Res., 117, B09311.

Gabriel, A.-A., J.-P. Ampuero, L. A. Dalguer, and P. M. Mai (2013), Source properties of dynamic rupture pulses with off-fault plasticity, J. Geophys. Res. 118, 4117-4126.

Gallovič, F., Ampuero, J.-P. (2015). A new strategy to compare inverted rupture models exploiting the eigen-structure of the inverse problem, Seism. Res. Lett., 86, 1679-1689.

Gallovič, F., Imperatori, W., Mai, P. M. (2015). Effects of three-dimensional crustal structure and smoothing constraint on earthquake slip inversions: case study of the Mw6.3 2009 L’Aquila earthquake, J. Geophys. Res. 120, 428-449.

Gallovič, F., Ľ. Valentová, J.-P. Ampuero, and A.-A. Gabriel (submitted). Bayesian Dynamic Finite-Fault Inversion: 1. Method and Synthetic Test, submitted to JGR.

Gallovič, F., and J. Zahradník (2012). Complexity of the Mw 6.3 2009 L’Aquila (Central Italy) earthquake: 1. Multiple finite-extent source inversion. J. Geophys. Res., 117, B04307.

Hallo, M., and F. Gallovič (2016). Fast and cheap approximation of Green functions uncertainty for waveform-based earthquake source inversions, Geophys. J. Int. 207, 1012-1029.

Harris, Ruth A., et al. (2018). A suite of exercises for verifying dynamic earthquake rupture codes. Seismological Research Letters 89.3 (2018): 1146-1162.

Huang, Y., and J.-P. Ampuero (2011), Pulse-like ruptures induced by low-velocity fault zones, J. Geophys. Res. 116, B12307.

Huang, Y., J. P. Ampuero, and D. V. Helmberger (2014). Earthquake ruptures modulated by waves in damaged fault zones J. Geophys. Res., 119 (4), 3133–3154.

Huang, M.-H., E. J. Fielding, C. Liang, P. Milillo, D. Bekaert, D. Dreger, and J. Salzer (2017). Coseismic deformation and triggered landslides of the 2016 Mw 6.2 Amatrice earthquake in Italy, Geophys. Res. Lett., 44, 1266-1274.

Cheloni, D., et al. (2017), Geodetic model of the 2016 Central Italy earthquake sequence inferred from InSAR and GPS data, Geophys. Res. Lett., 44, 6778–6787.

Kanamori, H., and E. E. Brodsky (2004). The physics of earthquakes, Reports Prog. Phys., 67, 1429-1496.

Kennett, B. L. N., and N. J. Kerry (1979). Seismic waves in a stratified half space. Geophys. J. Int., 57(3), 557-583.

Lanzano, G., Luzi, L., Pacor, F., Puglia, R., D'Amico, M., Felicetta, Ch., Russo, E. (2016). Preliminary analysis of the accelerometric recordings of the August 24th, 2016 MW 6.0 Amatrice earthquake, Ann. Geophys. 59, DOI: 10.4401/ag-7201.

Luzi, L., Puglia, R., Russo, E., D'Amico, M., Felicetta, C., Pacor, F., … Zaré, M. (2016a). The Engineering Strong-Motion database: A platform to access Pan-European accelerometric data. Seismological Research Letters, 87(4), 987–997.

Luzi, L., Puglia, R., Russo, E., & ORFEUS WG5 (2016b). Engineering Strong Motion Database, version 1.0, Istituto Nazionale di Geofisica e Vulcanologia. Observatories & Research Facilities for European Seismology. https://doi.org/10.13127/ESM

Madariaga, R., K. B. Olsen, and R. J. Archuleta (1998). Modelling dynamic rupture in a 3D earthquake fault model, Bull. Seismol. Soc. Am., 88, 1182-1197.

Mai, P. M., D. Schorlemmer, M. Page, J.-P. Ampuero, K. Asano, M. Causse, S. Custodio, W. Fan, G. Festa, M. Galis, F. Gallovič, W. Imperatori, M. Käser, D. Malytskyy, R. Okuwaki, F. Pollitz, L. Passone, H. N. T. Razafindrakoto, H. Sekiguchi, S. G. Song, S. N. Somala, K. K. S. Thingbaijam, C. Twardzik, M. van Driel, J. C. Vyas, R. Wang, Y. Yagi, O. Zielke (2016). The Earthquake-Source Inversion Validation (SIV) Project. Seism. Res. Lett., 87, 690-708.

Murphy, S., and S. Nielsen (2009). Estimating Earthquake Magnitude with Early Arrivals: A Test Using Dynamic and Kinematic Models, Bull. Seism. Soc. Am. 99, 1-23.

Oglesby, D. D., and S. M. Day (2002). Stochastic fault stress: Implications for fault dynamics and ground motion, Bull. Seism. Soc. Am. 92, 3006-3021.

Okada, Y. (1992). Internal deformation due to shear and tensile faults in a half-space, Bull. Seismol. Soc. Am. 82, 1018-1040.

Pacor, F., D. Spallarossa, A. Oth, L. Luzi, R. Puglia, L. Cantore, A. Mercuri, M. D'Amico, and D. Bindi (2016). Spectral models for ground motion prediction in the L'Aquila region (central Italy): Evidence for stress-drop dependence on magnitude and depth. Geophysical Journal International, 204(2), 697–718. http://doi.org/10.1093/gji/ggv448

Peyrat, S., and K. B. Olsen (2004). Nonlinear dynamic rupture inversion of the 2000 Western Tottori, Japan, earthquake, Geophys. Res. Lett., 31, L05604.

Pizzi, A., Di Domenica, A., Gallovič, F., Luzi, L., Puglia, R. (2017). Fault segmentation as constraint to the occurrence of the main shocks of the 2016 Central Italy seismic sequence, Tectonics 36, 2370-2387.

Ragon, T., A. Sladen, and M. Simons (2018). Accounting for uncertain fault geometry in earthquake source inversions – I: theory and simplified application, Geophys. J. Int. 214, 1174-1190.

Ragon, T., A. Sladen, and M. Simons (2019). Accounting for uncertain fault geometry in earthquake source inversions – II: application to the Mw 6.2 Amatrice earthquake, central Italy, Geophys. J. Int. 218, 689-707.

Ren, Y., H. Wang, and R. Wen (2017). Imprint of Rupture Directivity From Ground Motions of the 24 August 2016 Mw6.2 Central Italy Earthquake, Tectonics, 36, 3178-3191.

Ripperger, J., J.-P. Ampuero, M. P. Mai, and D. Giardini (2007). Earthquake source characteristics from dynamic rupture with constrained stochastic fault stress, J. Geophys. Res. 112, 1-17.

Ruiz, S., and R. Madariaga (2011). Determination of the friction law parameters of the Mw 6.7 Michilla earthquake in northern Chile by dynamic inversion, Geophys. Res. Lett., 38, L09317.

Sambridge, M. (2013). A Parallel Tempering algorithm for probabilistic sampling and multimodal optimization, Geophys. J. Int. 196, 357-374.

Tinti, E., Scognamiglio, L., Michelini, A., & Cocco, M. (2016). Slip heterogeneity and directivity of the ML 6.0, 2016, Amatrice earthquake estimated with rapid finite-fault inversion. Geophysical Research Letters, 43, 10,745–10,752.

Tung, S. and Masterlark, T. (2018). Resolving source geometry of the 24 August 2016 Amatrice, Central Italy, earthquake from InSAR data and 3D finite-element modeling, Bull. seism. Soc. Am.

Twardzik, C., S. Das, and R. Madariaga (2014). Inversion for the physical parameters that control the source dynamics of the 2004 Parkfield earthquake, J. Geophys. Res. Solid Earth, 119.

Ulrich, T., A. A. Gabriel, J. P. Ampuero, and W. Xu (2019). Dynamic viability of the 2016 Mw 7.8 Kaikoura earthquake cascade on weak crustal faults, Nature Comm. 10, 1213.

Viesca, R. C., and D. I. Garagash, (2015). Ubiquitous weakening of faults due to thermal pressurization. Nature Geoscience 8, 875-879.

Wollherr, S., A.-A. Gabriel, and P.M. Mai (2019). Landers 1992 "reloaded": Integrative dynamic earthquake rupture modeling. J. Geophys. Res., doi: 10.1029/2018JB016355.

A1 Appendix – validation of the best model

Here we compare rupture simulations calculated by the fast-speed FD3D code used in the inversion with the state-of-the-art code WaveQLab3D (Duru and Dunham, 2016) for the case of the best-fitting source model of the Amatrice earthquake (see Fig. 6 for the distribution of its dynamic parameter distribution). WaveQLab3D solves the 3D elastic wave equation in collocated curvilinear grids, where the spatial discretization uses high order accurate finite difference schemes satisfying the Summation-By-Parts rule (6th order accurate central finite difference stencils in the interior and one-sided 3rd order accurate at boundaries). The time discretization uses a 4th order accurate low-storage Runge-Kutta approach. Boundary conditions and frictional interfaces are imposed weakly using penalties, resulting in an energy-stable scheme. WaveQLab3D handles fault boundary conditions as tractions at split nodes and uses perfectly matched layers as absorbing boundaries. WaveQLab3D has been verified in many community dynamic rupture benchmarks (Harris et al., 2018). In the WaveQLab3D simulation we respect the actual fault geometry and dynamic normal stress changes. Comparing computational demands of the two codes, we find that while WaveQLab3D requires 6 hours on a recent 8-core CPU, FD3D only requires 10 minutes on a single-core CPU, i.e. the latter being ~300x faster.

Fig. A1A compares snapshots of the simulated rupture propagation. Fig. A1B compares the simulated waveforms. The main features of the rupture propagation are well captured by the FD3D solver. By experimenting we have found that the essential point is the mapping of the crustal model onto the approximate vertical fault plane to respect the spatial position of velocity model interfaces along the inclined fault. Furthermore, normal stress changes that are not accounted for when considering the vertical fault geometry (in FD3D) have only very minor effect on the rupture propagation in our case, in which the rupture has not reached the surface. WaveQLab tends to provide slightly faster rupture propagation for the given distribution of the dynamic parameters (and thus slightly larger waveforms), which we attribute to a better resolution of dynamic stress changes along the rupture front. Nevertheless, considering the extreme difference in the computational demands, we consider the agreements between the two solutions as satisfactory. Regarding the simulation speed, we note that due to the relative simplicity of the FD3D code, it was straightforwardly ported to GPU using OpenACC directives, which are implemented by the Portland Fortran compiler. The additional speed up of GPU (NVIDIA GTX Titan) vs the single-core CPU is about 5x, i.e. a single complete dynamic rupture simulation is performed within approximately 2 minutes.

Table 1 – Model and computational parameters considered for the 2016 Amatrice earthquake.

Parameter	***Value***
General	
Fault mechanism	Strike: 155°, dip: 45°, rake: -85°
Fault dimensions	Length 30 km, width 14 km
Fault top depth	0 km
Normal stress depth gradient	8.5 MPa/km
FD3D	
Spatial discretization	0.1 km
FD half-domain size (along strike x normal x along-dip)	300 x 100 x 140
Duration of slip-rate functions	10 s
Time step	0.002 s
Green's functions	
Spatial fault discretization	0.5 x 0.5 km
Time sampling	0.2 s
Waveform frequency range (displacements)	0.05 – 1.0 Hz (AMT, NRC) 0.05 – 0.5 Hz (other stations)
Model parameterization and prior ranges of parameters (homogeneous along the fault)	
Control point grid (along-strike x along-dip)	13 x 8
Pre-stress prior	0 – 100 MPa
Static – Dynamic friction coefficient prior	0 – 1.1
Characteristic slip-weakening distance prior	0.15 – 1.00 m
Nucleation area prior (along-strike, up-dip, radius)	16 km, 7 km, 4 km

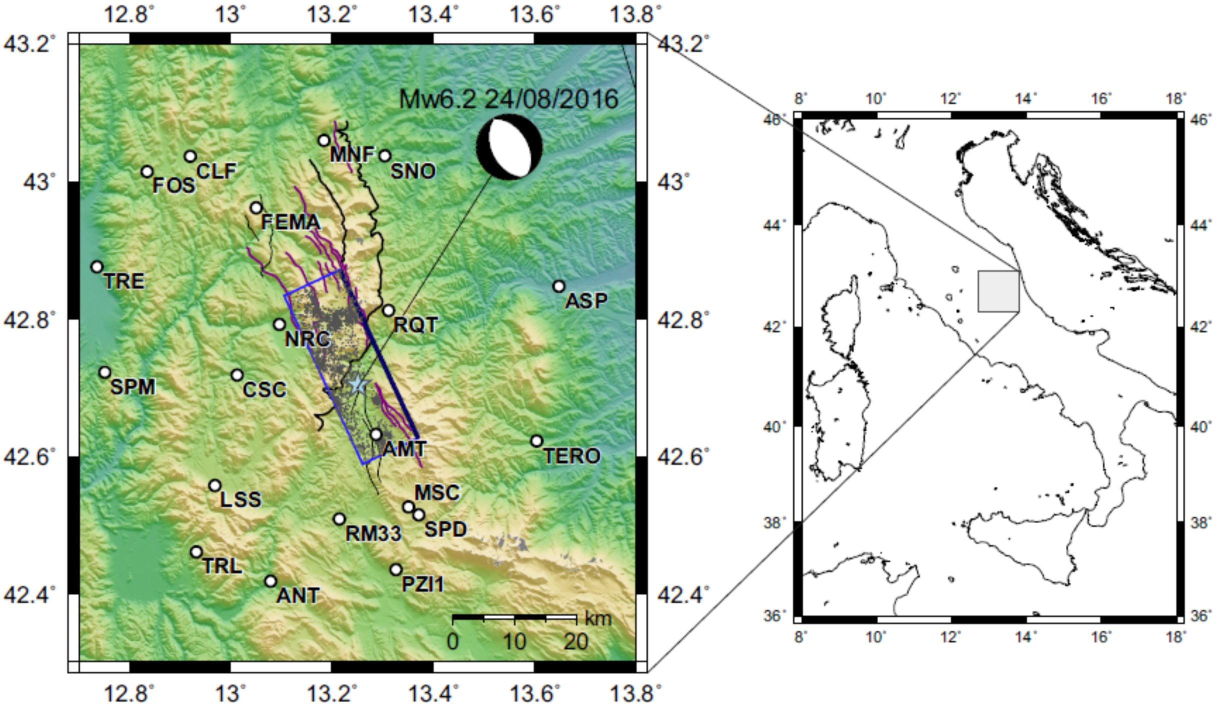

Figure 1: Map of Italy (right) with zoomed-in epicentral area of the 2016 Amatrice earthquake (left). The fault plane adopted from Pizzi et al. (2017) is shown by the rectangle (the thick line corresponds to the top edge at the surface). Stations are shown by white circles. The INGV mechanism and centroid location is shown by the beachball. Mainshock epicenter (light blue star) and on-fault aftershocks (grey dots) are taken from the relocated catalog by Chiaraluce et al. (2017). Black and red curves correspond to Miocene-Pliocene thrusts and active normal faults, respectively.

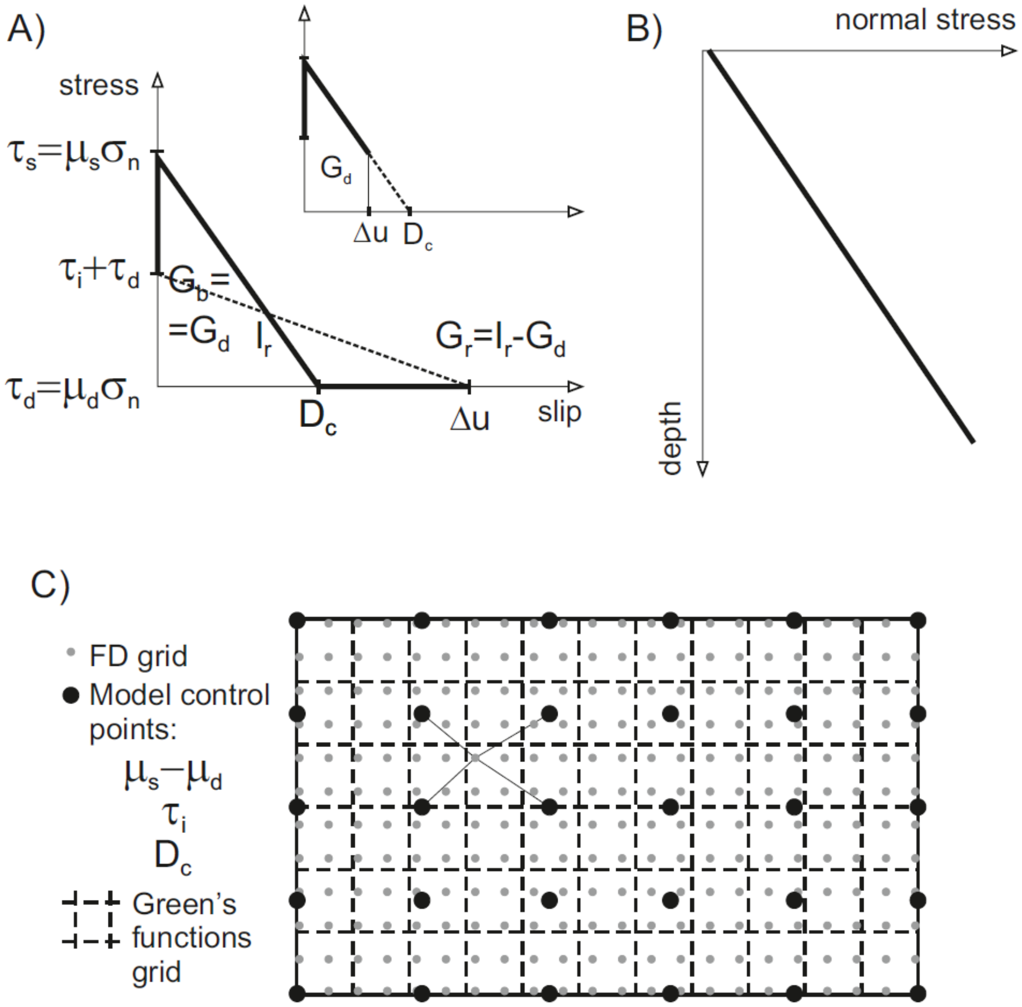

Figure 2: Rupture model and its parameterization. A) Linear slip-weakening friction law. Inverted parameters are prestress (initial stress) τ_i, difference between static and dynamic friction coefficients (μ_s-μ_d), and characteristic slip-weakening distance D_c. The frictional coefficient difference is converted to the respective breakdown stress drop by multiplication with a prescribed normal stress depth profile (B). G_b, G_d and G_r are break-down, dissipated break-down and radiated energy densities (Kanamori and Brodsky (2004), see text). Note that G_r is calculated as the difference between the dashed triangle and G_d. The inset illustrates situation when the slip does not reach D_c, i.e. when the break-down work and dissipated energies differ. (C) Illustration of three grids considered in the modeling. Model parameters are defined on the coarsest grid of control points. The values are bilinearly interpolated onto the densest finite-difference (FD) grid that is used by the FD3D dynamic rupture simulations. Slip rates calculated by FD3D are averaged spatially onto the coarser Green's functions grid, for which Green's functions are pre-calculated and stored. Waveforms are calculated by convolving the individual averaged slip rates with the respective Green's functions and summed, following the representation theorem. For the actual grid parameters considered in the present study see Tab. 1.

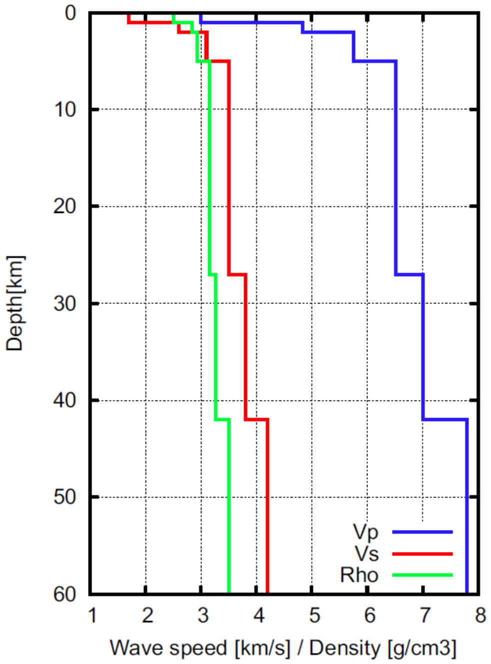

Figure 3: Velocity and density depth profile considered both in dynamic rupture simualtions and waveform calculations (Green’s functions). Adopted from Ameri et al. (2012).

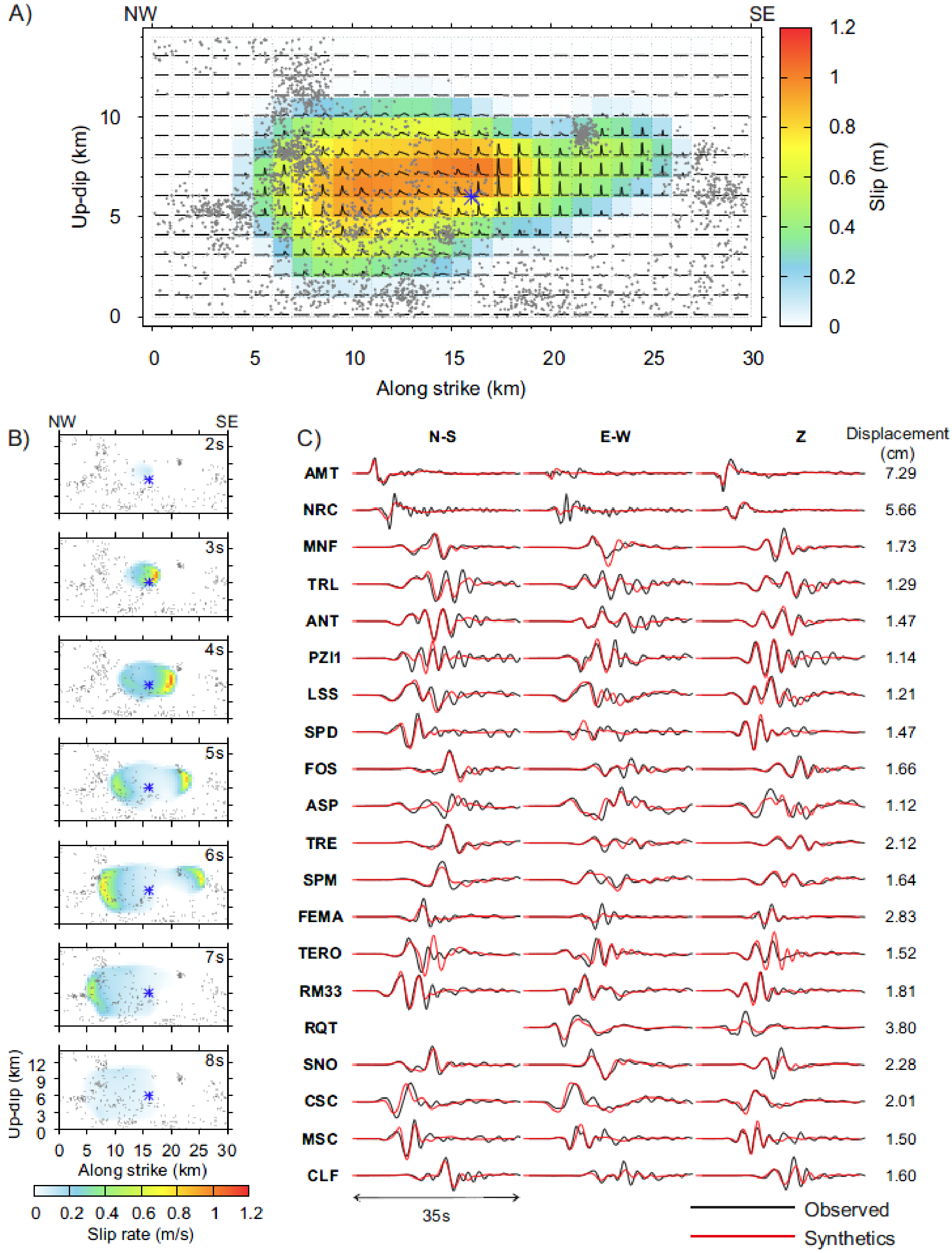

Figure 4: A) Slip distribution (color-coded) with superimposed slip rates of the best-fitting dynamic source model found by our dynamic inversion. Note that here for clarity the dynamic slip rates are shown on 1km x 1km grid, which is coarser than actually used in the waveform modeling. Star denotes the location hypocenter. B) Snapshots of slip rates showing the rupture propagation along the fault. Note that within the first 2 seconds (shown in Appendix in Fig. A1) the nucleation is so weak that the rupture almost ceases. In panels A and B the grey points mark the relocated on-fault aftershocks. C) Comparison between observed and synthetic data for the present model in frequency range 0.05-1.0Hz (AMT and NRC stations) and 0.05-0.5Hz (others). The variance reduction is 0.62.

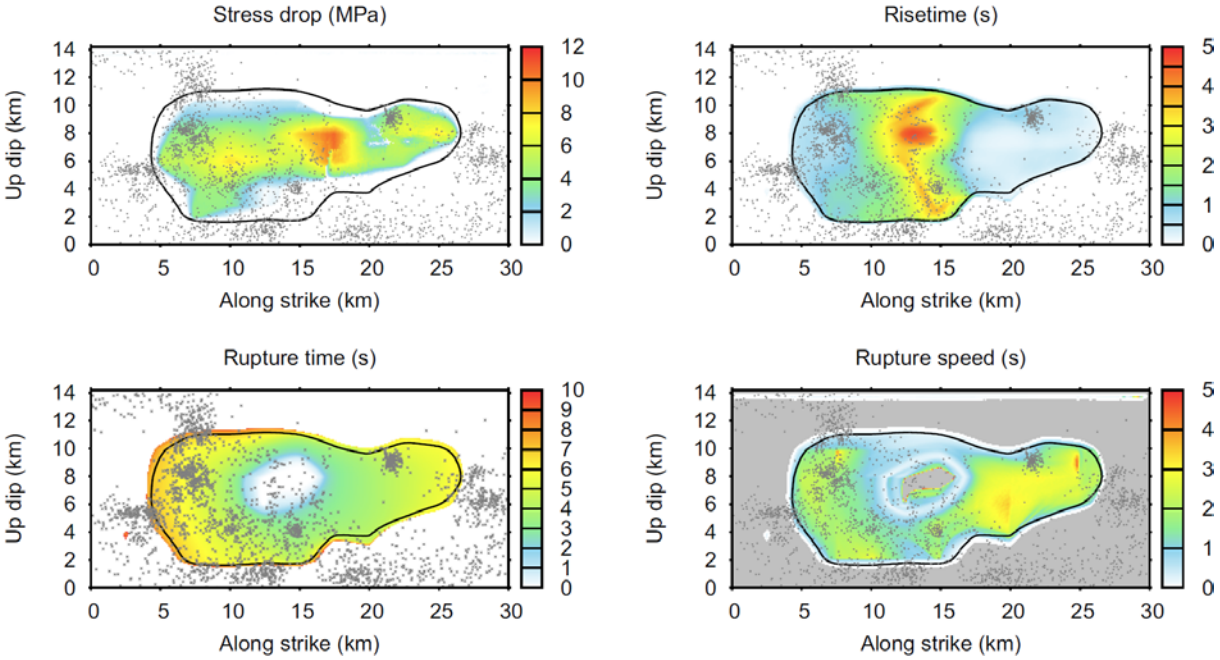

Figure 5: Kinematic parameters of the best-fitting model (see legend). Black contours delineate the slip distribution (see Fig. 4A). The grey points show the relocated on-fault aftershocks. The rupture speed (bottom right) is calculated locally from the distribution of rupture times (bottom left); grey masks areas with undetermined values.

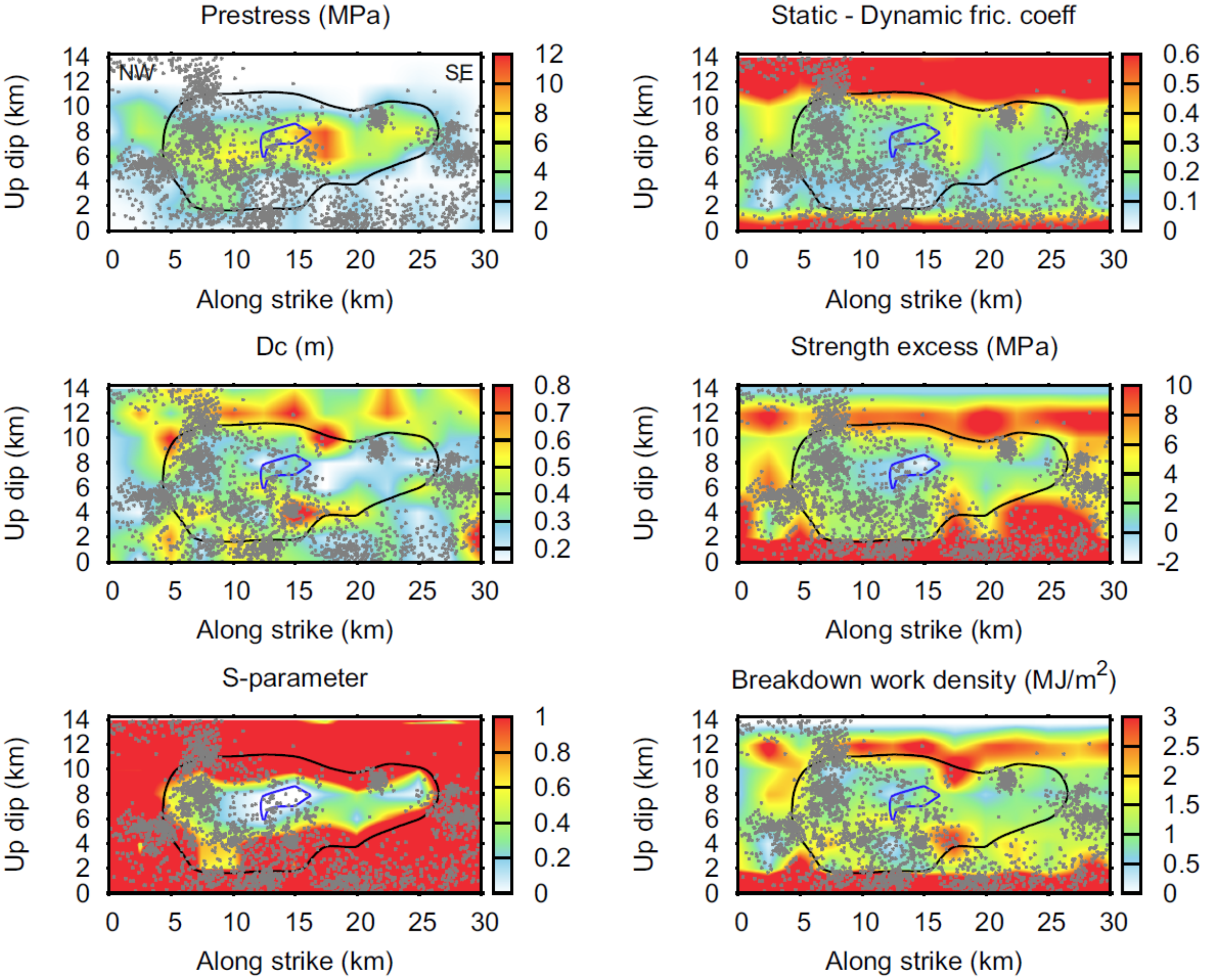

Figure 6: Dynamic parameters of the best-fitting model (see legend). Black and blue contours delineate the slip distribution (see Fig. 4A) and nucleation zone (having negative strength excess), respectively. The grey points show the relocated on-fault aftershocks.

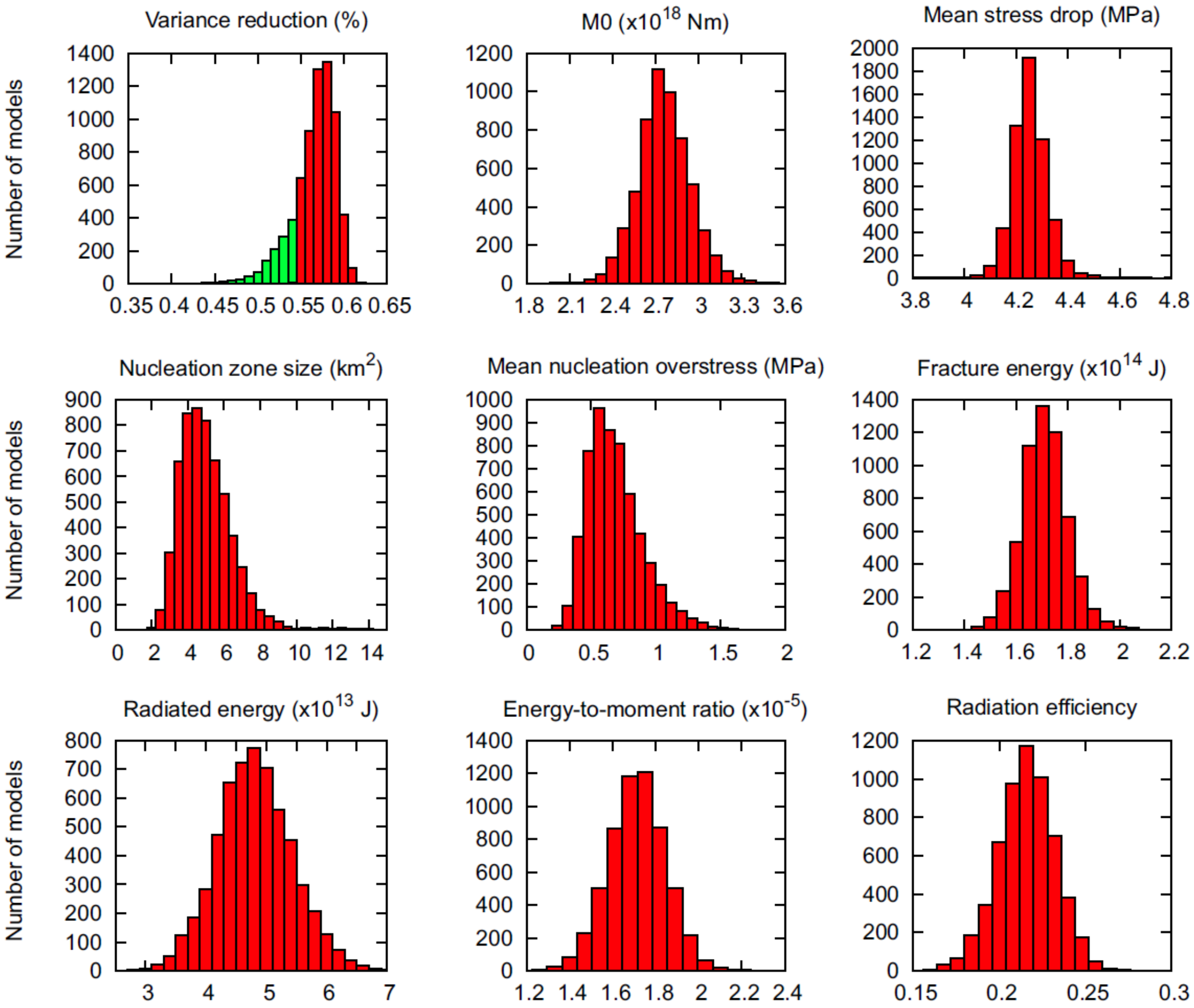

Figure 7: Histograms of rupture parameters as inferred by our Bayesian inversion considering models having posterior probability density value larger than 2% of the posterior PDF maximum (accepted models, in red). In the top left panel the combined red and green histogram corresponds to the variance reduction of all posterior model samples.

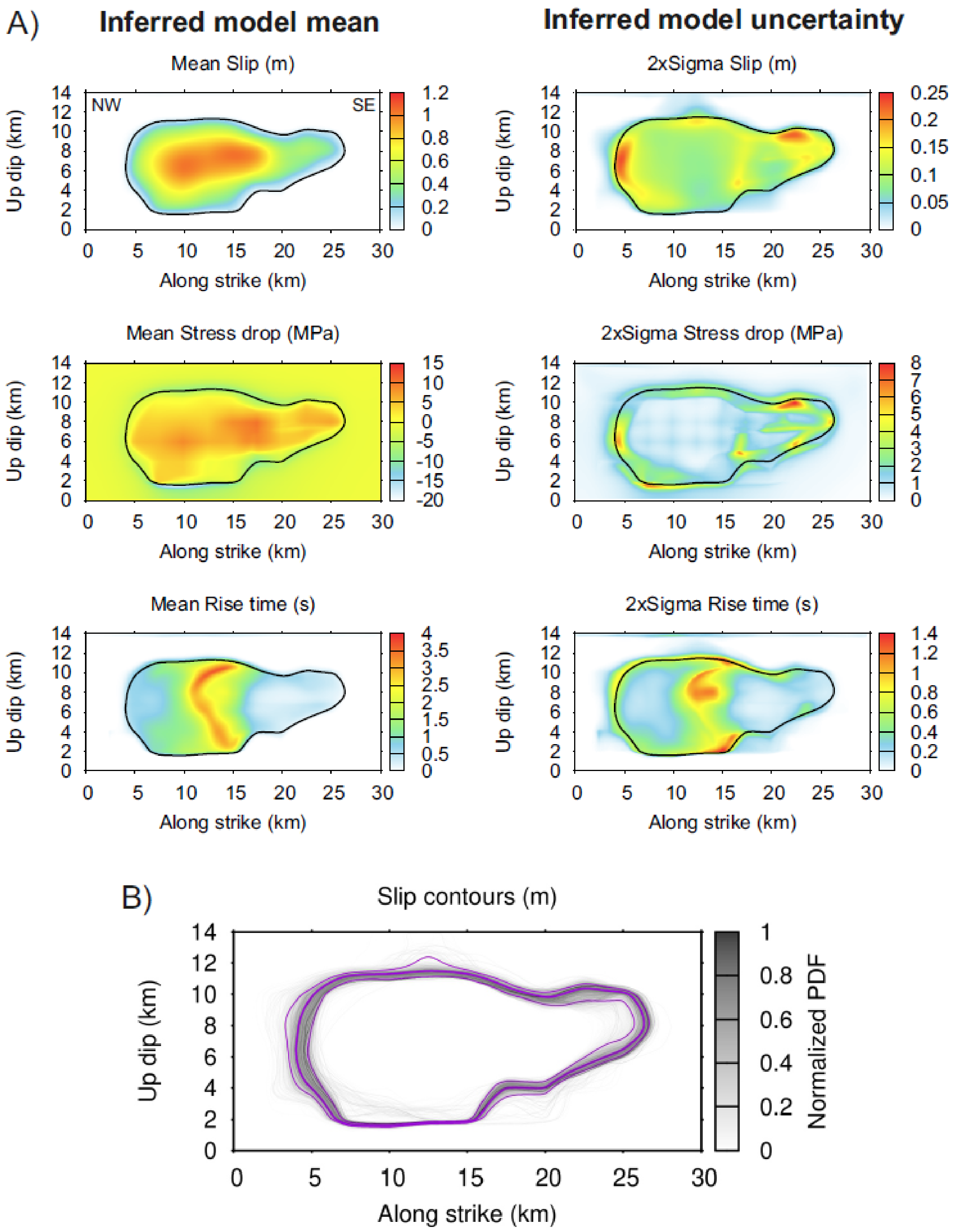

Figure 8: A) Rupture parameters inferred by the Bayesian dynamic inversion averaged over posterior samples (left) and the model parameters' uncertainty in terms of two sigma (right). B) Slip contours of all accepted posterior model samples coded in grey displaying the variability of the inferred spatial rupture extent. The thick and thin magenta lines show the contours of the averaged slip model and its two sigma uncertainty.

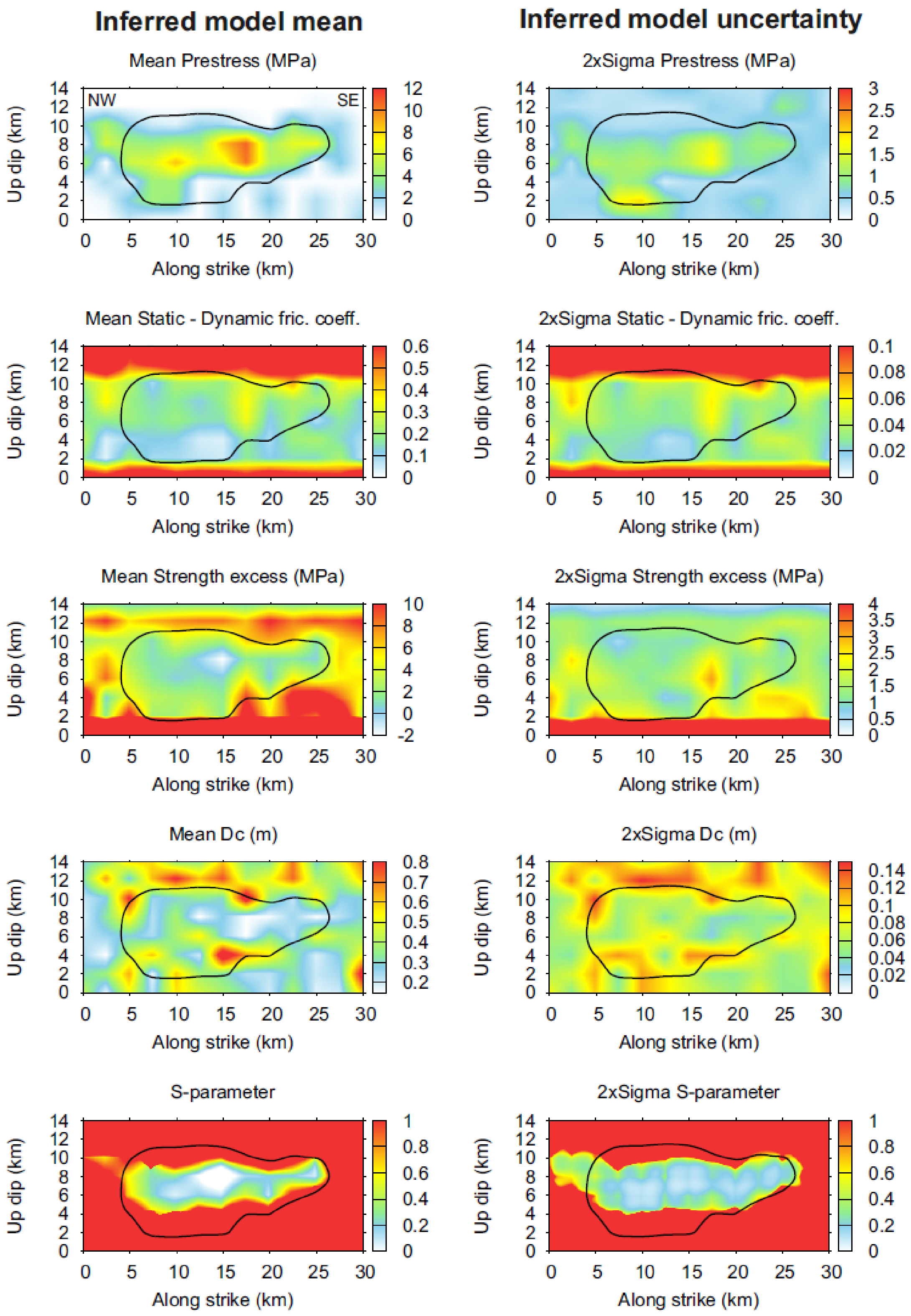

Figure 9: Distributions inferred dynamic parameters averaged over posterior samples (red) and their uncertainty in terms of two sigma. Black contour delineates the averaged slip distribution shown in Fig. 8A.

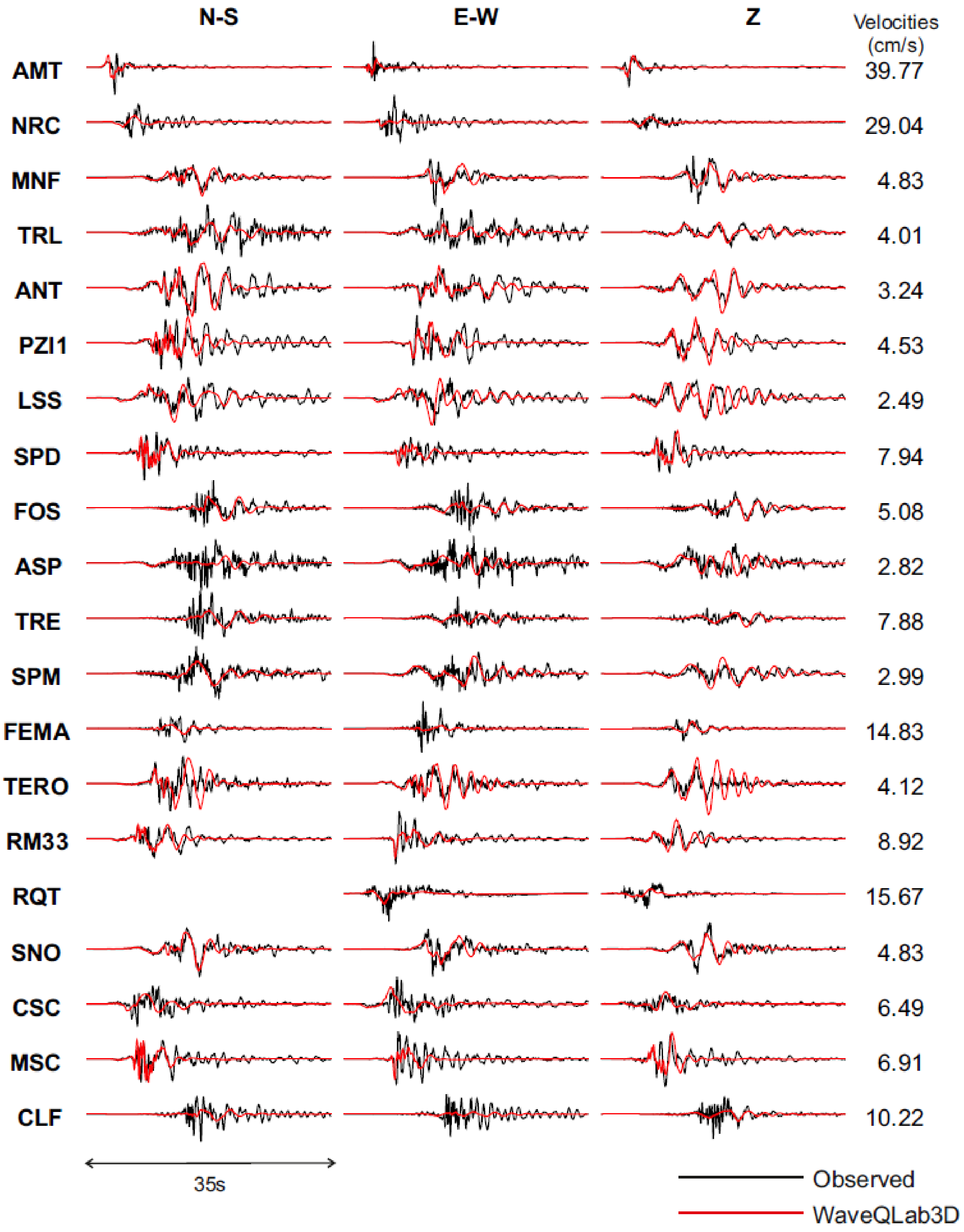

Figure 10: Comparison between observed (black) and synthetic (red) velocity waveforms for the best-fitting model of Fig. 4 calculated by WaveQLab3D in frequency range 0.05-5.0Hz. Note there is no additional alignment time shift of the individual waveforms.

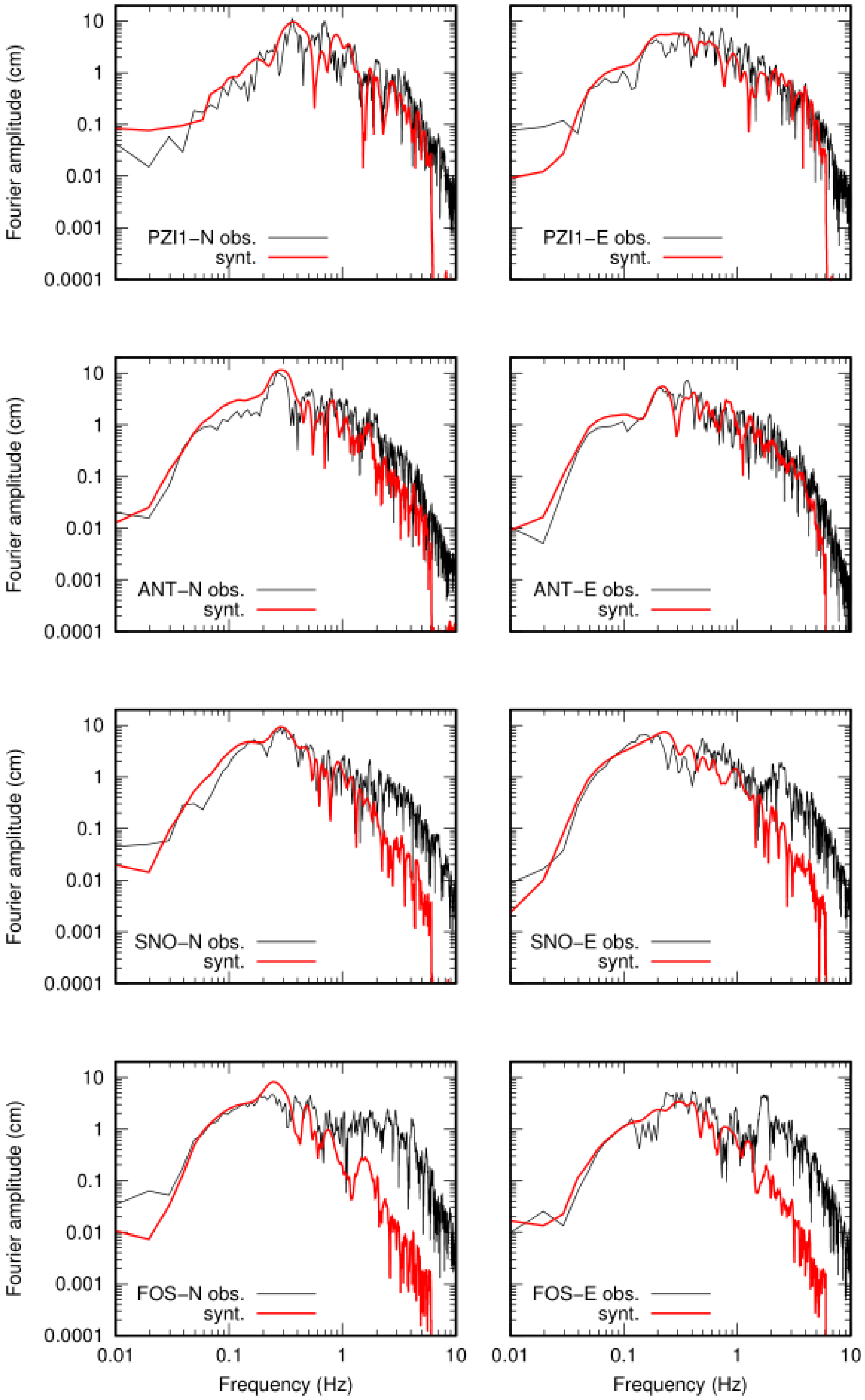

Figure 11: Comparison between Fourier spectra of observed (black) and synthetic (red) velocity waveforms for the best-fitting model of Fig. 4 calculated by WaveQLab3D in frequency range 0.05-5.0Hz for selected stations (rows) and components (columns). For comparison of their respective waveforms in time domain see Fig. 10. Note that the dynamic inversion was based only on the frequency range of 0.05-1Hz. The upper two rows represent examples of stations having presumably weak site-effects. Contrarily, the bottom two are affected by site-effect for frequencies larger than approximately 1Hz (see the abrupt change of the spectral decay slope).

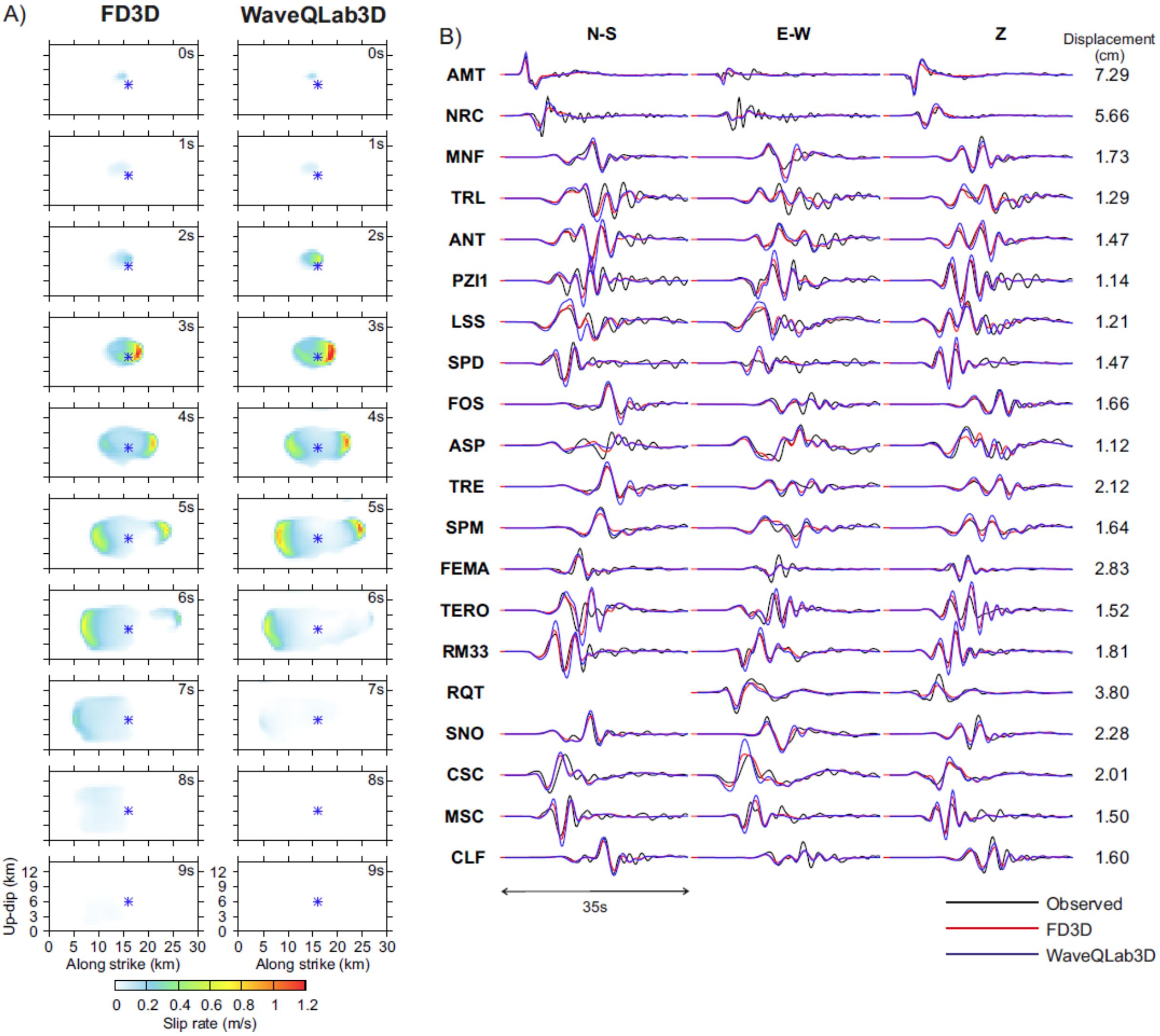

Figure A1: Validation of the best-fitting model of Fig. 4 using WaveQLab3D dynamic rupture simulation code by Duru and Dunham (2016). In WaveQLab3D the dipping fault geometry and the consequent dynamic normal stress variations are fully respected in the simulation, while in the FD3D the fault is approximated by a vertical plane to speed-up the calculation. The simulation results calculated by the two codes are compared in terms of: (A) slip-rate snapshots, and (B) displacement seismograms in the same frequency range as considered in the inversion (see Fig. 4B). The station names are depicted on the left (for their position see Fig. 1). Maximum amplitudes at the individual stations are shown on the right.